

This is the accepted manuscript made available via CHORUS. The article has been published as:

# Oxygen displacements and magnetoelectric coupling in $\text{LuMnO}_3$

P. Tong, Despina Louca, Nara Lee, and S.-W. Cheong

Phys. Rev. B **86**, 094419 — Published 14 September 2012

DOI: [10.1103/PhysRevB.86.094419](https://doi.org/10.1103/PhysRevB.86.094419)

# Oxygen displacements and magneto-electric coupling in LuMnO<sub>3</sub>

P. Tong,<sup>1\*</sup> Despina Louca<sup>1</sup> and Nara Lee<sup>2</sup>, S.-W. Cheong<sup>2</sup>

<sup>1</sup>*University of Virginia, Department of Physics, VA 22904, USA*

<sup>2</sup>*Rutgers Center for Emergent Materials and Department of Physics and Astronomy,  
Rutgers University, Piscataway, NJ 08854, USA*

(Dated: August 9, 2012)

The hexagonal multiferroic, LuMnO<sub>3</sub>, transforms to the  $P6_3cm$  symmetry upon entering the ferroelectric (FE) phase. Using neutron diffraction and the pair density function analysis, it is shown that short-range local atomic distortions are present, calling for a lower symmetry, such as the  $P6_3$ , for the following reasons: with cooling, the MnO<sub>5</sub> bipyramid tilting becomes more enhanced than previously determined. This splits the in-plane Mn-O-Mn angles especially below  $T_N$ , leading to inequivalent magnetic coupling constants,  $J$ , between the in-plane Mn ions. Additionally, below  $T_N$ , several weak incommensurate magnetic phases appear in response to the reminiscent frustration from the triangular Mn lattice. The complex magnetic structure may be the driving mechanism for the lower crystal symmetry.

PACS numbers: 75.85.+t, 61.05.F-, 61.50.Ks

The coexistence of competing order parameters in the class of materials referred to as the multiferroics is of great interest both from a fundamental point of view as well as for advancing new technologies<sup>1</sup>. The hexagonal manganites, AMnO<sub>3</sub> (A= rare earth ions with small radii such as Y, Lu, Ho, and Yb), with the crystal structure shown in Fig. 1(a) exhibit improper ferroelectricity and have provided a venue from which to explore the coupling of ferroelectric (FE) domains to antiferromagnetic (AFM) domains<sup>2-5</sup>. For this particular group of compounds, the ferroelectric transition,  $T_C$ , typically occurs at very high temperatures, around 1000 K, while the AFM transition,  $T_N$ , occurs at much lower temperatures,  $\sim 100$  K<sup>2-5</sup>. Upon cooling from the paraelectric phase with the  $P6_3/mmc$  symmetry, a structural transition occurs to the FE phase with the  $P6_3cm$  symmetry. In the latter symmetry, the center of inversion symmetry is absent, allowing for ferroelectric polarization to occur<sup>6</sup>. In contrast to some classic FE materials such as BaTiO<sub>3</sub> in which lattice distortions associated with the FE transition are typically large<sup>7</sup>, these are less obvious in the multiferroic compounds. In the hexagonal manganites, the FE phase is characterized by tilting of the MnO<sub>5</sub> bipyramids and buckling of the rare-earth layers<sup>8</sup>. The high temperature FE transition primarily arises from the displacement of the rare-earth ions with a minor contribution from the off-center motion of the Mn ions<sup>6,8</sup>. A key issue central to the magneto-electric interaction is to understand how the lattice evolves especially in the vicinity of  $T_N$ .

Since the FE transition is decoupled from the magnetic transition, the relationship between ferroelectricity and magnetism at  $T_N$  is in question. Early reports indicated that the magneto-elastic coupling is particularly weak at  $T_N \sim 100$  K in LuMnO<sub>3</sub>, the compound of interest in this study, because the magnetic coupling is predominantly in the  $ab$ -plane of the MnO<sub>5</sub> bipyramids while the electric dipole moments originating from the LuO<sub>7</sub> polyhedra are oriented along the  $c$ -axis<sup>9</sup>. Meanwhile,

previous results from neutron diffraction measurements on a series of hexagonal manganites, AMnO<sub>3</sub> (with A = Lu, Y, and Lu<sub>0.5</sub>Y<sub>0.5</sub>), suggested a possible isostructural transition at  $T_N$ , with unusually strong magneto-elastic coupling involving Mn<sup>10</sup>. The structural distortions reported in LuMnO<sub>3</sub> were the weakest of the three compounds studied. More recent reports on the local structure of HoMnO<sub>3</sub> determined from an X-ray absorption fine structure (XAFS) investigation suggested that the AFM transition coincides with a change of the Mn-Mn bond lengths in the  $ab$ - plane, further implying the presence of a spin-lattice coupling<sup>11</sup>.

Using high-resolution diffraction, we show that the crystal structure of LuMnO<sub>3</sub> is intricately related to a complex magnetic phase dramatically appearing below  $T_N$ . Using the neutron pair distribution function (PDF) analysis on a powder sample, we find that the local symmetry is lower than the reported  $P6_3cm$  symmetry in the temperature range from 10 to 300 K, as the local distortions are fit well using the lower symmetry of  $P6_3$  symmetry. The enhanced tilting of the MnO<sub>5</sub> bipyramids especially below  $T_N$  has a direct effect on the coupling of the in-plane Mn magnetism to the FE Lu-O polar bonds mediated via oxygen. The tilting consists of anti-directional displacements of the equatorial oxygen ions along the  $c$ -axis and anti-directional displacements of the apical oxygen ions in the  $ab$ -plane. The displacement of the equatorial oxygen ions largely breaks the geometric frustration of the triangular Mn lattice, allowing for a commensurate AFM order, and splits the Lu-O bonds along the  $c$ -axis. This may have an effect on the magnitude of the local electric dipoles. Below  $T_N$  however, several incommensurate magnetic phases appear along with the commensurate phase, which is evidence of the residual magnetic frustration of the Mn lattice. The complexity in the magnetic structure may be the driving force for the lower crystal symmetry.

The powder sample was prepared by standard solid state reaction following the method described in Ref.<sup>2</sup>.

The powder neutron diffraction measurements were performed as a function of temperature at the Neutron Powder Diffractometer (NPDF) of Los Alamos National Laboratory. The diffraction data were analyzed by the Rietveld method performed in reciprocal space and the PDF method of analysis carried out in real space. The diffraction data were corrected for instrumental background and sample container scattering, and were normalized by a vanadium standard<sup>12</sup>. Separately, absorption and multiple scattering corrections were applied as well. The structure function,  $S(Q)$ , obtained from the diffraction data where  $Q$  is the momentum transfer, was Fourier transformed to obtain the PDF,  $\rho(r)$ , as defined in<sup>13</sup>. The same data treatment was performed for all temperature sets while using the same termination  $Q_{max}$  of  $38 \text{ \AA}^{-1}$ . Since the PDF analysis includes both the Bragg and diffuse scattering intensities and does not assume a lattice periodicity, the PDF provides information on the short and medium-range order as well as on the displacements of atoms from their ideal sites.

The temperature dependence of the Bragg scattering intensity normalized using the (002) Bragg peak is shown in Fig. 2 (a-f). In the non-magnetic FE phase of 120 K, the diffraction pattern can be fit well with the  $P6_3cm$  symmetry. The refined parameters for this symmetry are listed in Table I, in agreement with published data. At  $T_N$ , shown in the second panel (b), several magnetic peaks appear some of which are labeled. The AFM structure takes the  $\Gamma_4$  configuration, which is shown in Fig. 1(c), and is the same as previously determined. Below  $T_N$ , several uncharacteristic magnetic effects are observed simultaneously with the commensurate AFM phase. The first is a broad, diffuse scattering intensity that appears  $\sim 1.85 \text{ \AA}^{-1}$  in a small temperature range that disappears before reaching 60 K (Fig. 1(c)). Below this temperature, new magnetic peaks emerge, corresponding to an incommensurate magnetic phase (I) that has not been indexed in spite of testing several models. This is shown in Fig. 1(e) at 40 K where the new peaks are identified with stars. With further cooling, the 40 K structure quickly disappears and a new incommensurate phase (II) appears as shown in Fig. 1(f) for data collected at 12 K. The appearance of the incommensurate phases is most likely related to the bump observed in the specific heat in Ref.<sup>5</sup> as well as the increasing susceptibility,  $\chi$ <sup>14</sup>, attributed to residual frustration in the system. Thus even below  $T_N$ , the spins are continuously fluctuating in search for the universal ground state. Future single crystal work will enable us to extract more detailed  $Q$  information on the incommensurate structures.

While, on average the crystal structure can be fit well with the  $P6_3cm$  symmetry, the local structure cannot be fit well using this symmetry. Shown in Fig. 3(a) is the PDF corresponding to the local structure for  $\text{LuMnO}_3$  at 12 K. The peaks in real space correspond to the probability of finding a particular pair of atoms at the given distance. The first two peaks with negative intensity, around 1.9 and 2  $\text{\AA}$ , correspond to the shortest Mn-O

bonds arising from the  $\text{MnO}_5$  bipyramids. These peaks are negative because of the negative neutron scattering length of Mn that is used to normalize  $\rho(r)$ <sup>15</sup>. Following is a strong positive peak at  $\sim 2.2 \text{ \AA}$  corresponding to Lu-O bonds, while the peak at  $\sim 2.9 \text{ \AA}$  corresponds to O-O bonds. The atomic coordinates for the average structure obtained from the Rietveld refinement based on the  $P6_3cm$  symmetry were used to calculate a model PDF shown as the solid line in the figure<sup>16</sup>. Overall, the fit of the experimentally determined PDF function to the one calculated from the average structure is good, but fails to reproduce the right peak shape at very short distances. In particular, small peaks at  $\sim 2.5$  and  $2.6 \text{ \AA}$  cannot be reproduced by the  $P6_3cm$  symmetry. The peak at  $2.6 \text{ \AA}$  has a lower intensity than expected from the model PDF. Furthermore, a mismatch in the peak intensity is observed at the Mn-O, Lu-O and O-O peaks, indicating that all atoms are involved in the local structural distortion.

To determine the origin of the local distortions, several subgroups of the  $P6_3cm$  symmetry were tested which led us to the  $P6_3$  symmetry. As seen in Fig. 3(b) at 12 K, the model calculated based on this symmetry can reproduce the experimentally observed PDF quite well. A comparison of the atomic coordinates obtained for the two space groups is shown in Table I. In the  $P6_3$ , all glide and mirror planes are absent, and the  $4b$  sites for Lu2, O3 and O4 sites are split creating an Lu3 site and an O5 site as shown in the crystal structure of Fig. 1(a). The partial PDFs from each atom pair based on the refined  $P6_3$  model are also shown in Fig. 3(b). It can be seen that the small peaks at  $\sim 2.5 \text{ \AA}$  and  $\sim 2.6 \text{ \AA}$  are attributed to Lu-O and O-O pairs, respectively. Also, the Mn-O bonds are more widespread, where the Mn-O peak is split to three instead of the two observed in the average model.

The evolution of the local structure with temperature is shown in Fig. 3(c). The PDF peaks become sharper with decreasing temperature due to the suppression of atomic thermal motion, as expected. Although the peak shapes do not change, it is nonetheless interesting to observe that the peak height of different bonds exhibit different temperature dependences. Fig. 3(d) is a plot of the PDF peak height relative to the peak height value at 300 K for the Mn-O (at  $\sim 1.9 \text{ \AA}$ ), Lu-O (at  $\sim 2.2 \text{ \AA}$ ) and O-O (at  $\sim 2.9 \text{ \AA}$ ) peaks. While the Mn-O peak height shows almost no temperature dependence, the O-O peak changes gradually with temperature while the Lu-O peak exhibits the strongest change on approaching  $T_N$ . All changes appear to saturate below  $T_N$ . The changes in the PDFs with temperature cannot be simply understood in terms of thermal motion, and a reconstruction of the local atomic distortions is needed to explain this temperature dependence as described below. This is done using the  $P6_3$  symmetry.

The results from the local structure refinement are summarized in Fig. 4. The evolution of the bond lengths with temperature indicates significant changes. In the

$P6_3$  symmetry, there are five Mn-O bond pairs in the  $\text{MnO}_5$  bipyramid due to the splitting of the O4 sites to O4 and O5. All Mn-O bonds change at  $T_N$  as seen in Fig. 4(a) and (b) plotted in the same range. It is the long Mn-O5 bond that separates from the others and approaches the Lu-O peak with increasing temperature. The shift of the Mn-O5 bond leads to a cancellation of the negative intensity from this pair with the positive Lu-O peak intensity as seen in Fig. 3. In Fig. 4(c) and (d), the temperature dependence of all Lu-O bonds is shown. The Lu1-O2, Lu1-O3, Lu2-O1, Lu2-O4, Lu3-O1, and Lu3-O5 pairs show most dramatic changes at  $T_N$ , either in the form of a bond contraction or expansion. Thus it is the wide distribution in the Lu-O bond lengths that reduces the sharpness of the Lu-O peak at low temperatures as shown in Fig. 3(d). This explains the saturation of the Lu-O peak intensity below  $T_N$ .

In the  $P6_3$  structure, the  $\text{MnO}_5$  bipyramids are tilted due to nearly antiparallel displacements of the in-plane O1 and O2 atoms, and anti-parallel displacements of the O3, O4 and O5 atoms along the  $c$ -axis. The tilting is characterized by two angles,  $\alpha$ , which is the angle between the O3-O4-O5 plane and the basal plane, and  $\beta$  which is a vertical angle marking the deviation away from the  $c$ -axis of the plane between O1-O2 (Fig. 1(b)). As shown in Fig. 5(a), the resulting angles  $\alpha$  and  $\beta$  increase with decreasing temperature and saturate below  $T_N$ , indicating a magneto-elastic coupling associated with the magnetic transition.

In  $\text{LuMnO}_3$ , the AFM ground state is determined by the Mn lattice since the Lu ion is not magnetic. At low temperatures, the locally distorted lattice lifts the degeneracy of the ground state, and helps stabilize the long-range AFM order<sup>18</sup>. It was previously shown that the in-plane AFM superexchange coupling is dominant while the interlayer interactions are two orders of magnitude weaker<sup>17</sup>. The in-plane superexchange between nearest Mn atoms is mediated by intermediate oxygen atoms via the nearly  $120^\circ$  Mn-O-Mn channel as shown in Fig. 1(c). From our data we infer that there are three distinct Mn-O-Mn channels since the O4 site splits to two, giving rise to three magnetic coupling,  $J$ , constants with different magnitudes. From Fig. 5(b), it can be seen that the bond angles change below  $T_N$ , where the Mn-O4-Mn and Mn-O5-Mn with similar angles are separated from the Mn-O3-Mn bond angle. This indicates that there are two similar in magnitude  $J$  constants and a very different third one. Indeed, two different in-plane magnetic couplings were observed in a recent inelastic neutron scattering measurement with very different energies, -4.09 meV and -1.54 meV<sup>17</sup>. In contrast, in the average structure, the two in-plane Mn-O-Mn angles ( $118.59^\circ$  and  $118.12^\circ$ ) are very close to each other, which cannot explain the two well distinct  $J$ 's.

The  $c$ -axis off-center displacements of the O3, O4 and O5 atoms are significant in the electric polarization. Surrounding each Lu atom are seven oxygen atoms, forming seven Lu-O bonds of various lengths. The electric po-

larization in the  $P6_3$  unit cell is only allowed along the  $c$ -axis as in the  $P6_3cm$  symmetry which is parallel to the sixfold screw axis, while all in-plane polarizations cancel each other out. Along the  $c$ -axis, there are three types of O-Lu-O chains: the O3-Lu1-O3, O4-Lu3-O5 and O5-Lu2-O4. The dipole moment is proportional to the displacement of the Lu atom relative to the center of its two neighboring O atoms in an O-Lu-O chain. What we found is that in each chain, the O and Lu atoms are displaced in opposite directions and by different magnitudes, leading to inequivalent Lu-O bonds (Fig. 4(c)). The direction of motion is indicated in Fig. 1(a). Therefore, electric dipoles formed along the O3-Lu1-O3 chain have a different direction from those along the O4-Lu3-O5 and O5-Lu2-O4 chains (Fig. 4(a)), reducing the total electric polarization. This is analogous to an AFM structure with a weak magnetization due to antiparallel moments at different sites.

To summarize, we find that the local structure of  $\text{LuMnO}_3$  can be well described by the  $P6_3$  symmetry, a lower symmetry from the currently used  $P6_3cm$  for this system. Locally, an isosymmetric transition occurs at  $T_N$  with dramatic changes in atomic displacements and bond lengths. The tilting of the  $\text{MnO}_5$  bipyramids due to the off-centering of surrounding oxygen atoms increases with decreasing temperature and saturates below  $T_N$ . The enhanced local distortions below  $T_N$  largely lift the frustration and allow for the in-plane AFM coupling. In addition, the off-center displacement of the equatorial oxygen ions (O3, O4 and O5) in the  $\text{MnO}_5$  bipyramids is closely associated with the local electric polarization via the Lu bonding. To conclude, our results suggest that the local structure can serve as a powerful method in exploring the magneto-electric coupling in multiferroic materials.

This work is supported by the U. S. Department of Energy under contracts DE-FG02-01ER45927 at the University of Virginia and by DE-FG02-07ER46382 at Rutgers.

\*Current address: Key Laboratory of Materials Physics, Institute of Solid State Physics, Hefei 230031, People's Republic of China

Table I. The lattice parameters and atomic coordinates determined from the Rietveld refinement for  $P6_3cm$  and from the local structure refinement for the  $P6_3$  symmetry at 12 K. In  $P6_3cm$ , the coordinates are  $(0, 0, z_{\text{Lu1}})$ ,  $(1/3, 2/3, z_{\text{Lu2}})$ ,  $(x_{\text{Mn}}, 0, 0)$ ,  $(x_{\text{O1}}, 0, z_{\text{O1}})$ ,  $(x_{\text{O2}}, 0, z_{\text{O2}})$ ,  $(0, 0, z_{\text{O3}})$  and  $(1/3, 2/3, z_{\text{O4}})$ . In the  $P6_3$ , Lu2 splits into  $(1/3, 2/3, z_{\text{Lu2}})$  and  $(1/3, 2/3, z_{\text{Lu3}})$  with  $z_{\text{Lu3}} \sim 0.5 + z_{\text{Lu2}}$ , and O4 splits into  $(1/3, 2/3, z_{\text{O4}})$  and  $(1/3, 2/3, z_{\text{O5}})$  with  $z_{\text{O5}} \sim 0.5 + z_{\text{O4}}$ . The other coordinates are  $(x_{\text{Mn}}, y_{\text{Mn}}, 0)$ ,  $(x_{\text{O1}}, y_{\text{O1}}, z_{\text{O1}})$  and  $(x_{\text{O2}}, y_{\text{O2}}, z_{\text{O2}})$ . The coordinates for Lu1 and O3 remain the same as in  $P6_3cm$ .

$P6_3\text{cm}$		$P6_3$	
a,b(Å)	6.0286(1)	a,b(Å)	6.0287(6)
c (Å)	11.3627(2)	c (Å)	11.3845(5)
$z_{Lu1}$	0.2767(8)	$z_{Lu1}$	0.2674(6)
$z_{Lu2}$	0.2317(2)	$z_{Lu2}$	0.2130(8)
		$z_{Lu3}$	0.7256(8)
$x_{Mn}$	0.3317(2)	$x_{Mn}$	0.3144(5)
		$y_{Mn}$	-0.0245(0)
$x_{O1}$	0.3051(8)	$x_{O1}$	0.2971(2)
		$y_{O1}$	-0.0057(3)
$z_{O1}$	0.1646(9)	$z_{O1}$	0.1578(8)
$x_{O2}$	0.6377(5)	$x_{O2}$	0.6468(3)
		$y_{O2}$	0.0078(2)
$z_{O2}$	0.3367(7)	$z_{O2}$	0.3366(0)
$z_{O3}$	0.4754(3)	$z_{O3}$	0.4646(1)
$z_{O4}$	0.0213(4)	$z_{O4}$	0.0172(9)
		$z_{O5}$	0.5054(0)

- 
- <sup>1</sup> W. Erenstein, N. D. Mathur and J. F. Scott, *Nature* (London) **442**, 759 (2006); S.-W. Cheong and M. Mostovoy, *Nat. Mater.* **6**, 13 (2007); R. Ramesh and N. A. Spaldin, *Nature Mater.* **6**, 21 (2007).
  - <sup>2</sup> T. Katsufuji, S. Mori, M. Masaki, Y. Moritomo, N. Yamamoto and H. Takagi, *Phys. Rev. B* **64**, 104419 (2001).
  - <sup>3</sup> M. Fiebig, Th. Lottermoser, D. Frölich, A. V. Goltsev and R. V. Pisarev, *Nature* (London) **419**, 818 (2002).
  - <sup>4</sup> H. Sugie, N. Iwata and K. Kohn, *J. Phys. Soc. Jpn.* **71**, 1558-1564 (2002).
  - <sup>5</sup> D. G. Tomuta, S. Ramakrishnan, G. J. Nieuwenhuys and J. A. Mydosh, *J. Phys. Condens. Matter* **13**, 4543-4552 (2001).
  - <sup>6</sup> I.-K. Jeong, N. Hur and Th. Proffen, *J. Appl. Cryst.* **40**, 730-734 (2007).
  - <sup>7</sup> G. H. Kwei, A. C. Lawson and S. J. L. Billinge, *J. Phys. Chem.* **97**, 2368 (1993).
  - <sup>8</sup> B. B. Van Aken, T. T. M. Palstra, A. Filippetti and N. A. Spaldin, *Nature Mater.* **3**, 164 (2004).
  - <sup>9</sup> B. B. Van Aken and T. T. M. Palstra, *Phys. Rev. B* **69**, 134113 (2004).
  - <sup>10</sup> S. Lee, A. Pirogov, M. Kang, K.-H. Jang, M. Yonemura, T. Kamiyama, S.-W. Cheong, F. Gozzo, N. Shin, H. Kimura, Y. Noda and J.-G. Park, *Nature* (London) **451**, 805 (2008).
  - <sup>11</sup> T. A. Tyson, T. Wu, K. H. Ahn, S.-B. Kim and S.-W. Cheong, *Phys. Rev. B* **81**, 054101 (2010).
  - <sup>12</sup> B. H. Toby, *J. Appl. Cryst.* **34**, 210 (2001).
  - <sup>13</sup> B. E. Warren, H. Krutter and O. Morningstar, *J. Am. Ceram. Soc.* **19**, 202 (1936).
  - <sup>14</sup> A. Muñoz, J. A. Alonso, M. J. Martínez-Lope, M. T. Casáis, J. L. Martínez, M. T. Fernández-Días, *Phys. Rev. B* **62**, 9498 (2000).
  - <sup>15</sup> D. Louca and T. Egami, *Phys. Rev. B* **59**, 6193 (1999).
  - <sup>16</sup> C. L. Farrow, P. Juhas, J. W. Liu, D. Bryndin, E. S. Božin, J. Bloch, Th Proffen and S. J. L. Billinge, *J. Phys.: Condens. Matter* **19**, 335219 (2007).
  - <sup>17</sup> H. J. Lewtas, A. T. Boothroyd, M. Rotter, D. Prabhakaran, H. Müller, M. D. Le, B. Roessli, J. Gavilano and P. Bourges, *Phys. Rev. B* **82**, 184420 (2010).
  - <sup>18</sup> X. Fabrèges, S. Petil, I. Mirebeau, S. Paihès, L. Pinsard, A. Forget, M. T. Fernandez-Diaz and F. Porcher, *Phys. Rev. Lett.* **103**, 067204 (2009).

Figure captions:

Fig.1. (Color online) (a) The crystal structure of  $P6_3$  at 12K. The arrows indicate the displacement direction. (b) The tilting of the  $\text{MnO}_5$  bipyramids is defined using two angles: the angle  $\alpha$  is the tilting angle of the basal plane; the angle  $\beta$  is the tilting angle away from the  $c$ -axis for O1 and O2 atoms. The arrows represent the atomic displacements away from the ideal positions in the high-temperature paraelectric phase. (c) The antiferromagnetic spin configuration shown with two Mn layers, viewed down from the  $c$ -axis.

Fig.2. (Color online) The neutron diffraction patterns at various temperatures. The nuclear peaks are indexed with  $P6_3cm$  symmetry at 120K. The magnetic peaks can be attributed to the  $k=0$  antiferromagnetic order at 90 K. At 40K, new diffraction peaks show up (star). Below 30K, a different set of Bragg peaks appear (cross). The new peaks are magnetic in nature because they disappear at higher temperatures.

Fig.3. (Color online) (a) A comparison of the average  $P6_3cm$  model and the experimental PDF at 12 K. The vertical bars indicate the bond positions from Rietveld refinement. (b) A comparison of the  $P6_3$  model with the same experimental PDF at 12 K. The partial PDFs calculated from the  $P6_3$  model corresponding to different bond pairs are shown as well. (c) The temperature dependent of the local structure. (d) The PDF peak height as a function of temperature for the Mn-O (at  $\sim 1.9$  Å), Lu-O (at  $\sim 2.2$  Å) and O-O (at  $\sim 2.9$  Å) peaks marked in (a).

Fig.4. (Color online) The temperature dependence of Mn-O bonds (a), (b), and Lu-O bonds (c)-(d). Sharp changes are observed at  $T_N$ .

Fig.5. (Color online) (a) The tilting angles  $\alpha$  and  $\beta$  as a function of temperature. (b) The in-plane Mn-O3-Mn, Mn-O4-Mn and Mn-O5-Mn angles as a function of temperature.



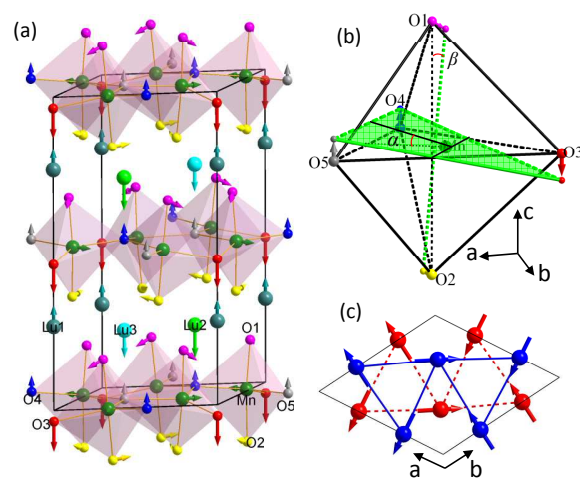


Figure 1. Tong et al.,



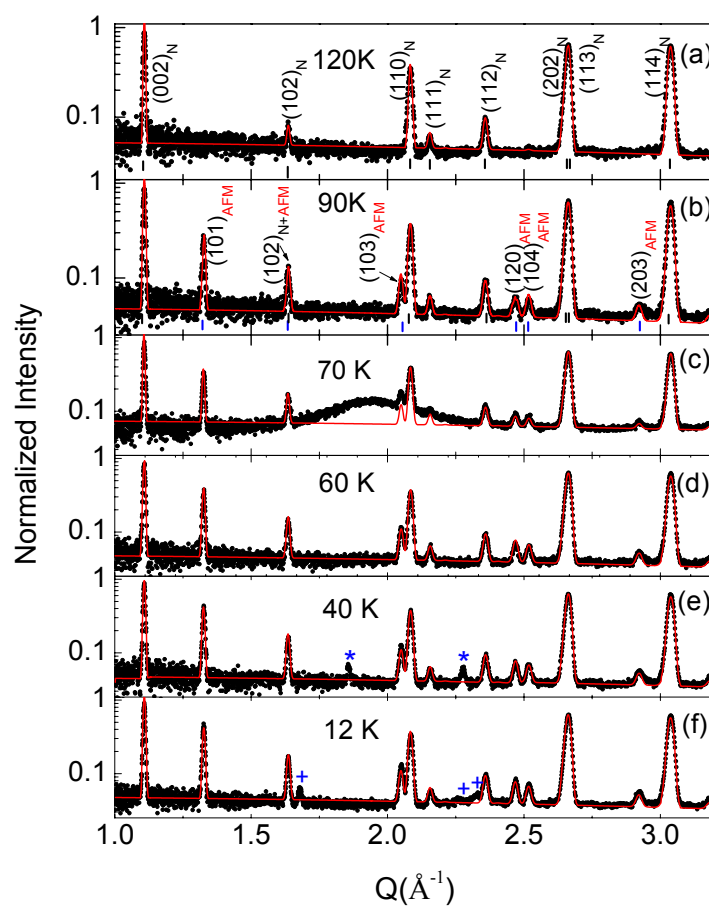


Figure 2. Tong et al.,

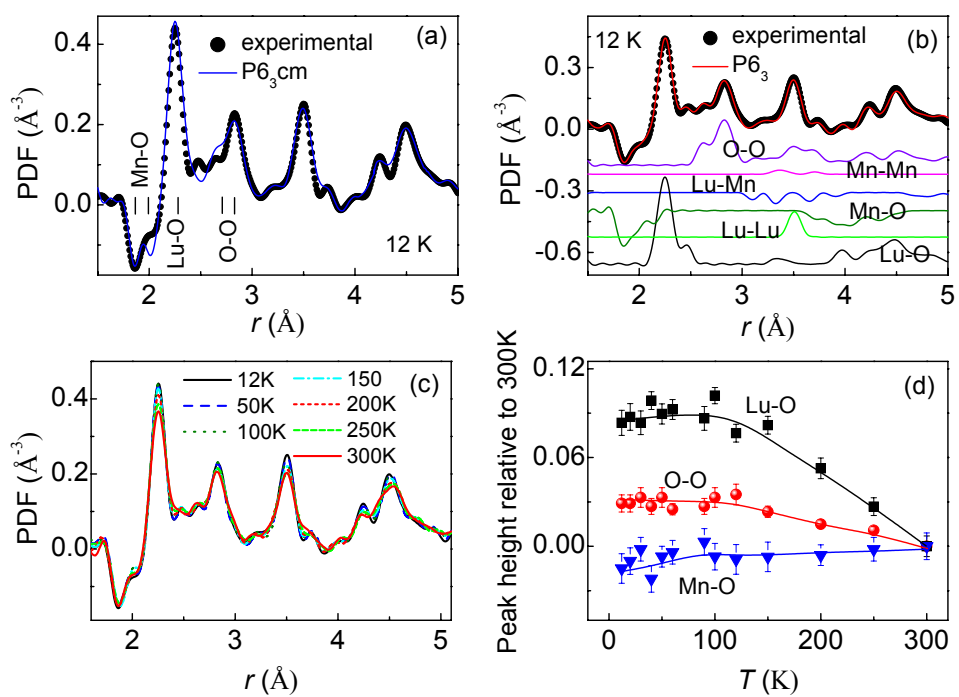


Figure 3. Tong et al.,

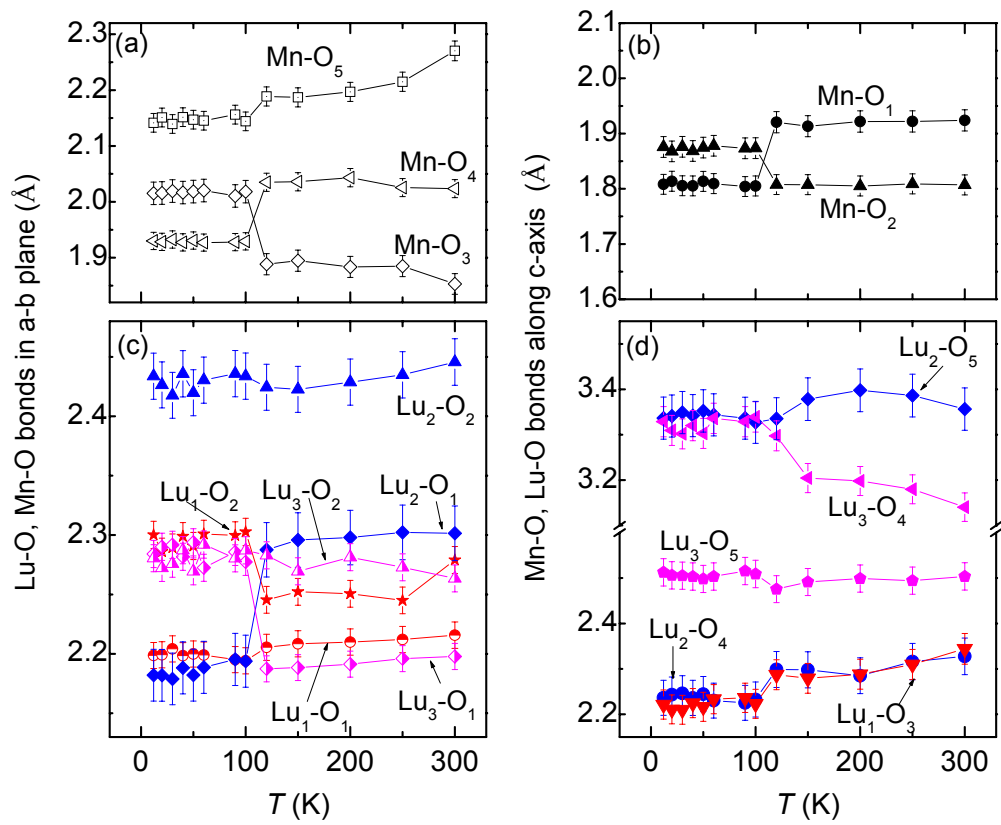


Figure 4. Tong et al.,

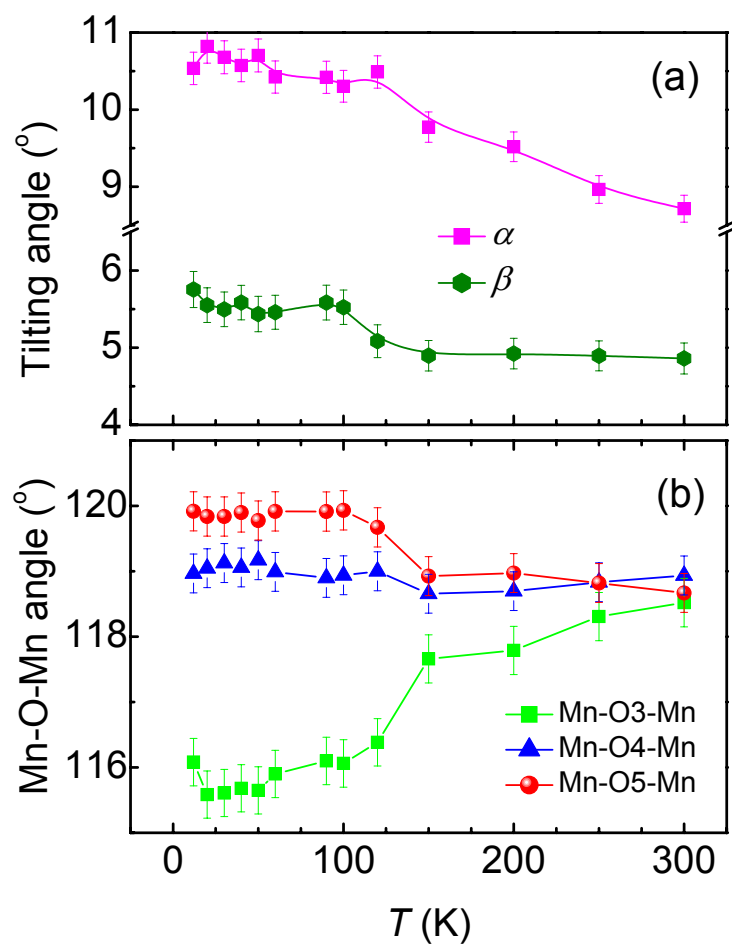


Figure 5. Tong et al.,